

# Contrast Mechanisms for the Detection of Ferroelectric Domains with Scanning Force Microscopy

Tobias Jungk,\* Ákos Hoffmann, and Elisabeth Soergel  
*Institute of Physics, University of Bonn,  
Wegelerstraße 8, 53115 Bonn, Germany*

(Dated: October 29, 2018)

We present a full analysis of the contrast mechanisms for the detection of ferroelectric domains on all faces of bulk single crystals using scanning force microscopy exemplified on hexagonally poled lithium niobate. The domain contrast can be attributed to three different mechanisms: i) the thickness change of the sample due to an out-of-plane piezoelectric response (standard piezoresponse force microscopy), ii) the lateral displacement of the sample surface due to an in-plane piezoresponse, and iii) the electrostatic tip-sample interaction at the domain boundaries caused by surface charges on the crystallographic  $y$ - and  $z$ -faces. A careful analysis of the movement of the cantilever with respect to its orientation relative to the crystallographic axes of the sample allows a clear attribution of the observed domain contrast to the driving forces respectively.

PACS numbers: 68.37.Ps, 77.84.-s, 77.65.-j

## I. INTRODUCTION

In the last decade, piezoresponse force microscopy (PFM) has become a standard technique for imaging ferroelectric domains [1, 2, 3]. This is mainly due to its ease of use and nonetheless high lateral resolution of  $< 20$  nm without any special sample preparation [4]. PFM is based on the fact that ferroelectric materials are necessarily piezoelectric [5]. Application of electric fields causes thickness changes of the ferroelectric sample via the converse piezoelectric effect. For PFM a scanning force microscope (SFM) is operated in contact mode with a voltage applied to the conductive tip. The thickness change induced by the electric field of the tip is followed by the tip and leads to a deflection of the cantilever that can be read-out as a vertical signal on the segmented photo-detector. Because the thickness changes are in the order of a few ten picometers an alternating voltage is applied to the tip and the oscillations of the cantilever are read-out with a lock-in amplifier. This contrast mechanism, based on the longitudinal piezoelectric effect, is generally used in PFM measurements and will be named "standard PFM" in the following.

In contrast to other visualization techniques [6] PFM is not restricted to specific crystallographic orientations. Recording the torsion of the cantilever (a lateral signal on the segmented photo-detector), thereby mapping an in-plane movement of the sample surface, enables to record a domain structure also on crystal faces not exhibiting an out-of-plane response due to a longitudinal piezoelectric tensor element. An example is the visualization of the domain structure on the non-polar face in periodically poled  $\text{KTiOPO}_4$  single crystals [7].

Obviously, it is most appropriate to record the ver-

tical and the lateral signal simultaneously to obtain as much information as possible on the domain structure of the sample. First experiments using this detection scheme were carried out on bulk barium titanate crystals [8, 9]. Only a few studies on other bulk crystals exhibiting  $a$ - and  $c$ -domains were reported ever since ( $\text{Bi}_4\text{Ti}_3\text{O}_{12}$  [10, 11],  $\text{PbTiO}_3$  [12],  $\text{SrBi}_2\text{Ta}_2\text{O}_9$  [13], PZN-PT [14], and PMN-PT [14, 15]). After all there are also a few publications where simultaneous recording of the vertical and the lateral signals on thin films is reported ( $\text{BiFeO}_3$  [16],  $\text{LiNbO}_3$  [17],  $\text{PbTiO}_3$  [18, 19, 20], and PZT [21, 22]).

In order to obtain full information on the domain configuration of a crystal surface exhibiting  $a$ - and  $c$ -domains, however in general, one single scan recording both read-out channels is not sufficient. The vertical signal clearly distinguishes  $+c$ - and  $-c$ -domains. The lateral signal depicts the in-plane  $a$ -domains. These, however, can be oriented in four directions ( $\leftarrow \mid \uparrow \mid \rightarrow \mid \downarrow$ ). Since within one image only two in-plane orientations of the polarization ( $\rightleftharpoons$  or  $\uparrow\downarrow$ ) can be distinguished a second image of the same area after rotation by  $90^\circ$  is necessary to determine the domain configuration completely. The crucial point for such investigations is the relocation of the sample position after rotation. In case of samples with distinct topographic features this is relatively easy and was performed on polycrystalline particles of  $\text{BiFeO}_3$  [23],  $\text{LaBGeO}_5$  [20] or thin film capacitors with top electrodes [24]. But also for samples with no specific topography, images at different angles were recorded [9, 13, 16, 19, 20, 23, 24].

The contrast in the lateral channel is generally attributed to a shear movement of the sample caused by non-diagonal elements of the piezoelectric tensor driven by the out-of-plane component of the electric field  $E_\perp$  from the tip [8, 14, 21, 25]. Our measurements, however, strongly support a different explanation: a sliding movement of the surface induced by the in-plane components

---

\*Electronic address: jungk@uni-bonn.de

of the electric field  $E_{\parallel}$  together with an in-plane longitudinal piezoelectric tensor element  $d$ . Although the electric field from the tip is rotational symmetric the crystal deformations  $\Delta t$  caused by the opposed in-plane electric field components  $E_{\parallel}$  do not cancel out:  $\Delta t = E t d$ , where  $t$  denotes the thickness of the crystal and the direction of  $E$  determines whether  $\Delta t$  is positive or negative, i. e. resulting in an expansion or a contraction of the crystal respectively.

In this contribution we present a thorough investigation of PFM imaging on all crystal faces of hexagonally poled lithium niobate (LiNbO<sub>3</sub>) crystals. All faces show a distinct domain contrast, which on the  $x$ - and  $y$ -faces strongly depends on the relative orientation of the cantilever with respect to the crystallographic axes. Three different contrast mechanisms were found to contribute to the measured signals: (i) vertical piezoresponse of the sample causing deflection of the cantilever (standard PFM), (ii) lateral piezoresponse resulting in torsion and buckling on top of the domain faces and (iii) electrostatic forces also leading to torsion and buckling, however only at the domain boundaries [26]. For a clear attribution of the respective driving forces the angle between the cantilever and the crystallographic axes must be known. We therefore upgraded our PFM setup with a high precision PC-controlled rotation stage. Performing angular-dependent measurements of the vertical and the lateral signals – both recorded simultaneously – on all three crystal faces we could determine the surface displacements on each crystal face causing the domain contrast.

This paper is organized as follows: Because the experimental challenges are demanding we start with a detailed description of the experimental methods (Sec. II). The next section describes the experimental results (Sec. III). Here we firstly focus on our proposed model to explain a sliding of the surface underneath the tip causing the domain contrast on the  $x$ - and the  $y$ -faces (Sec. III A). Since this model has not been described so far, but in contrary a different driving mechanism is generally assumed to cause the surface deformation, this section will be very detailed. In the following section (Sec. III B) we present the experimental results to sustain the proposed surface deformations by imaging all-faces of a two-dimensionally poled lithium niobate crystal. The last section (Sec. III C) focusses once more of  $y$ -face imaging, showing most obviously the proposed contrast mechanisms.

## II. EXPERIMENTAL METHODS

For the experiments we used a commercial scanning force microscope (SMENA from NT-MDT) modified to allow the application of voltages to the tip, and thus to be utilized as piezoresponse force microscope. The instrument is operated in contact mode with an alternating voltage applied to the tip ( $U = 5 \text{ V}_{\text{rms}}$ ,  $f = 30 - 60 \text{ kHz}$ ), the backside of the sample being grounded.

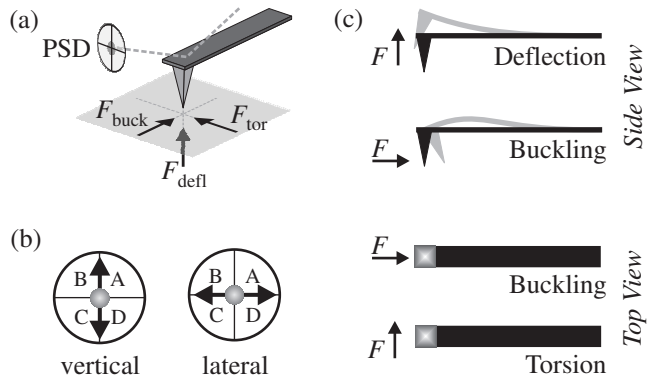


FIG. 1: (a) Forces acting on the tip leading to deflection ( $F_{\text{defl}}$ ), torsion ( $F_{\text{tor}}$ ), and buckling ( $F_{\text{buck}}$ ). (b) Deflection and buckling are detected as vertical signals whereas torsion results in a lateral signal. (c) The out-of-plane force  $F_{\text{defl}}$  leads to a deflection of the cantilever which is independent of its orientation with respect to the surface. For the in-plane forces  $F_{\text{tor}}$  and  $F_{\text{buck}}$  the response of the cantilever depends crucially on its orientation with respect to the driving forces. PSD: position sensitive detector.

In Sec. II A we will describe the possibilities for read-out of the cantilever movements. The excitation of the movements depends on the orientation of the driving forces with respect to the cantilever axis. We therefore upgraded our SFM setup with a rotation stage described in the following section (Sec. II B). In addition we separately investigated the friction between tip and sample (Sec. II C) and performed an accurate cross-talk compensation (Sec. II D). Finally, we briefly summarize the properties of LiNbO<sub>3</sub> relevant for understanding the origin of the domain contrast in SFM measurements, and in particular present the sample we used for the experiments (Sec. II E).

### A. Movements of the cantilever

Basically the cantilever can perform three independent movements: (i) deflection due to an out-of-plane force  $F_{\perp}$  acting along the axis of the tip, (ii) torsion caused by an in-plane force  $F_{\parallel}$  acting perpendicular to the cantilever axis and (iii) buckling if an in-plane force  $F_{\parallel}$  acts along the cantilever axis (Fig. 1(a,c)). Deflection is independent on the orientation of the cantilever with respect to the sample. An in-plane force  $F_{\parallel}$  acting on the tip results in torsion  $F_{\text{tor}} = F_{\parallel} \sin \alpha$  and buckling  $F_{\text{buck}} = F_{\parallel} \cos \alpha$  of the cantilever. Here  $\alpha$  denotes the angle between  $F_{\parallel}$  and the cantilever axis. Thus, a rotation of the sample by  $90^{\circ}$  transforms a torsion signal into a buckling signal and vice versa.

Unfortunately a separate readout of all three signals is not possible since both deflection and buckling are detected in the same read-out channel as a vertical signal (Fig. 1b). Torsion, however, can clearly be distinguished as it is read-out as a lateral signal. In order to deter-

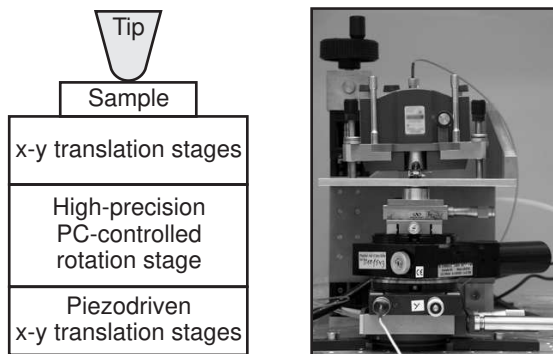


FIG. 2: Schematics (left) and photo (right) of the setup for angular dependent measurements. The piezo-driven translation stages at the bottom allow a precise positioning of the rotation axis with respect to the tip. The translation stages on top of the rotation stage are used to position the sample.

mine whether a vertical signal is caused by deflection or by buckling, one has to perform measurements at different angles  $\alpha$ . All angular dependent contributions to the vertical signal can then be attributed to buckling movements. To get the full picture on the piezoelectric responses of the sample we recorded PFM data at different angles  $\alpha$  with two lock-in amplifiers, thus measuring vertical and lateral signals simultaneously.

### B. Rotation sample stage

In order to determine the direction of the in-plane driving force  $F_{\parallel}$  acting on the tip, angular resolved measurements were carried out. We therefore put the SFM on a home-built lifting platform and mounted the sample on a high-precision, PC-controlled rotation stage (Newport URM80). The latter was mounted on top of two piezo-driven translation stages in order to position its rotation axis precisely underneath the tip (Fig. 2). The obtained accuracy was such that on a full revolution the tip describes a circle of  $< 3 \mu\text{m}$  radius on the surface. Another set of translation stages, mounted on top of the rotation stage, was used to position the sample underneath the tip. The whole setup was found to be stable enough to operate the SFM while rotating the sample.

In this setup the adjustment of the pivot of the rotation stage with respect to the position of the tip is very crucial. It has to be repeated for every new cantilever since its mounting is not precise to an accuracy of a few microns. For a coarse alignment the displacement of a  $20 \mu\text{m}$  wide cross was observed during rotation with the help of an optical microscope. By repeated adjustment of the pivot after  $180^\circ$  rotations an accuracy of approx.  $20 \mu\text{m}$  was achieved. The fine alignment was conducted with a periodically poled  $\text{LiNbO}_3$  (PPLN) sample with a domain width of  $4 \mu\text{m}$ . Comparing two PFM images recorded before and after rotating the sample by  $180^\circ$  allowed to determine the misalignment and thereafter to correct it

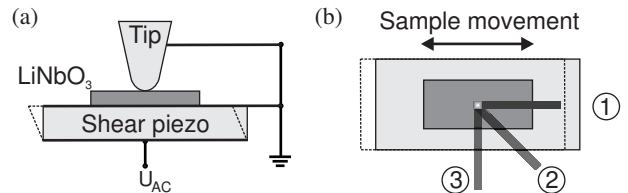


FIG. 3: (a) Test-setup for determining the friction between tip and  $\text{LiNbO}_3$  crystal surface. (b) Three selected orientations of the cantilever. In ① only buckling can be observed, in ③ the cantilever is oriented such that torsion occurs and ② shows the situation for exciting both movements.

with the piezo-driven translation stages underneath the rotation stage (Fig. 2).

This setup allows to record SFM images at specific angles between the cantilever and the crystallographic axes of the sample. Furthermore, we could obtain angular dependent measurements with the tip stationary, named "rotation scans" in the following. They were carried out with the help of a LabView program addressing the rotation stage as well as the lock-in amplifiers. For data acquisition we waited  $100 - 1000 \text{ ms}$  at every new angle ( $10\times$  the time constant of the lock-in amplifier) to let the microscope calm down from the braking of the rotation stage.

### C. Friction between tip and sample

Because in-plane forces act on the tip, special attention has to be paid to the friction between tip and sample surface. Therefore we realized a test setup depicted in Fig. 3(a) where we mounted a single domain  $\text{LiNbO}_3$  crystal on top of a shear piezo driven with an alternating voltage  $U_{AC}$ . In order to avoid any electrostatic forces between tip and sample, both were grounded. In this configuration, only in-plane forces act on the tip, resulting in torsion and/or buckling of the cantilever, depending on the relative orientation between the sample movement and the cantilever axis (Fig. 3(b)). The tip was found to follow the surface movement perfectly for an amplitude  $A < 300 \text{ pm}$  and a frequency  $f < 100 \text{ kHz}$ .

### D. Cross-talk compensation

The aim to accurately attribute the measured signals to the respective driving forces requires the cross-talk-free detection of the vertical and the lateral signals. Usually, however, due to a misalignment between the plane of the read-out laser beam and the orientation of the position sensitive detector, the two signals are not fully separated. The setup with the shear piezo can be used to adjust for the cross-talk with the tip being in contact with the sample. Torsion and buckling can be excited separately through the shear piezo movement along with

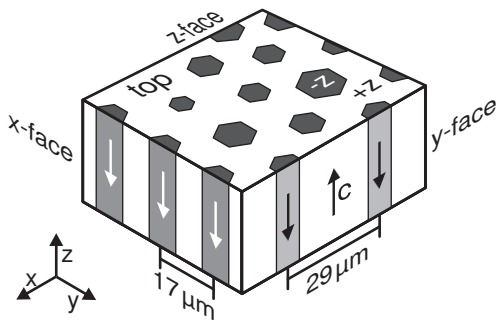


FIG. 4: Schematics of the hexagonally poled LiNbO<sub>3</sub> sample (HexLN) used for the investigations. All faces are optically polished. The periodicity of the corresponding PPLN structures on the side faces are indicated together with the orientation of the polar  $c$ -axis.

the angular adjustment using the rotation stage. The false signals caused by cross-talk are then electronically suppressed [27]. This way of cross-talk compensation is advantageous insofar, as it is performed under the same conditions as the measurements carried out later on.

### E. Sample and sample preparation

The experiments were carried out with congruently melting lithium niobate crystals (LiNbO<sub>3</sub>). Here, we briefly summarize the crystals main properties: The surface polarization charge on the  $z$ -face is  $P_s = 0.7 \text{ C/m}^2$  [28]. This value being very high, a compensation of the charges takes place, which is assumed [29] and experimentally verified [26] to be of the order of a factor of 1000. This value strongly depends on the exact crystal composition as well as the environmental conditions, i. e. mainly humidity. We also have evidence for surface charging on the  $y$ -faces which is of the order of  $\frac{1}{3}$  to  $\frac{1}{4}P_s$ . Although this has not been explicitly reported so far, however, it has already been observed [30] and it is also very possible from theoretical considerations [31]. We claim the presence of a surface charging on the  $y$ -face because of the observation of long-range ( $> 10 \mu\text{m}$ ) forces during tip-sample approach. The latter was found to behave similar than on the  $z$ -face but completely different from non-charged surfaces like glass or the  $x$ -face of LiNbO<sub>3</sub>. Furthermore the contrast observed at the domain boundaries on the  $y$ -faces (Secs III B, III C) can only be explained by a domain specific surface charging [26].

Because of being ferroelectric, LiNbO<sub>3</sub> is also piezoelectric and the piezoelectric coefficients can be found in the literature [28]:  $d_{22} = 21 \text{ pm/V}$ ,  $d_{33} = (6-21) \text{ pm/V}$ ,  $d_{15} = 69 \text{ pm/V}$  and  $d_{31} = -1 \text{ pm/V}$ . We would like to point out three facts:

- There is no longitudinal piezoelectric tensor element along the  $x$ -axis ( $d_{11} = 0$ ).
- For the longitudinal piezoelectric tensor element

$d_{33}$  along the  $z$ -axis, the reported values vary considerably (by a factor of three).

- The values given above apply for bulk crystals in a homogeneous electrical field, i. e. samples covered with large top electrodes. In the case of PFM, however, the tip acts as top electrode, leading to a strongly inhomogeneous electric field expanding only a few microns into the crystal. As a consequence, clamping reduces the electromechanical response of the crystal. Since clamping depends on elasticity, this effect is not the same for all crystal orientations. We measured the ratio between the longitudinal piezoelectric coefficients as they are determined by PFM using single domain  $y$ - and  $z$ -cut samples to be  $d_{22} : d_{33} = 1 : 5$ .

For the experiments we used a two-dimensionally periodically poled lithium niobate (LiNbO<sub>3</sub>) crystal as depicted in Fig. 4. All faces were optically polished. The different period lengths of the domain structures on the  $x$ - and on the  $y$ -faces allow a unambiguous identification of the face under investigation. The sample size was  $(5 \times 7 \times 0.5) \text{ mm}^3$ .

To exclude any effect from a possible mis-orientation of the sample cuts relative to the crystallographic axes, we also prepared samples where half of the  $x$ - and  $y$ -faces were polished at angles of  $5^\circ$  and  $10^\circ$ . However, the slants did not affect the results.

During the experiments it turned out that special care has to be taken of the mounting of the sample. The lock-in detection technique being extremely sensitive, any inhomogeneity of the grounding electrode was observed to have an influence on the measured signals, presuming an angular dependence when rotating the sample. For the measurements on the  $z$ -face, the crystal was simply led on a large metal plate (2 cm diameter). For investigating the side faces we mounted the sample with the help of two additional plastic brackets.

## III. EXPERIMENTAL RESULTS

In order to avoid a misunderstanding in the following we would like to point out some basics here. Applying a voltage  $U$  to a piezoelectric sample of thickness  $t$  leads to an electric field  $E = U/t$  inside that sample causing a piezoelectric deformation  $\Delta t = E dt = U d$  with  $d$  being the appropriate piezoelectric tensor element. Depending on the direction of  $E$  the sample experiences contraction ( $\Delta t < 0$ ) or expansion ( $\Delta t > 0$ ). The same applies also in case of an inhomogeneous electric field, like the one generated by the tip of the PFM, since  $\int_0^t E ds = U$  [32].

### A. Movements of the sample surface

Applying a voltage  $U$  to the tip results in a first approximation in a radial field distribution when approximating

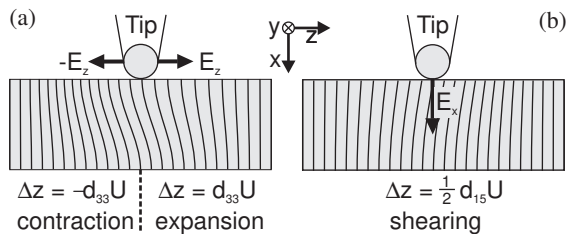


FIG. 5: Possible origins for the lateral movement of the  $x$ -surface of a single domain LiNbO<sub>3</sub> sample underneath the tip (applied voltage  $U$ ). In (a) the deformation of the crystal is due to a contraction and an expansion caused by the electrical field components  $\pm E_z$ . (b) Shearing caused by the electric field component  $E_x$  is strongly suppressed by clamping.

the tip by a sphere. Usually in PFM, only the out-of-plane component  $E_{\perp}$  of the electric field, perpendicular to the sample surface and thus along the axis of the tip is taken into account, causing a thickness change of the sample. A few publications also discuss shear deformations of the sample caused by  $E_{\perp}$  [8, 14, 20, 21, 25]. All other components of the electric field  $E_{\parallel}$  in plane of the sample surface are generally presumed to cancel out due to rotational symmetric considerations. This argument, however, does not hold. In contrary, the contributions of the piezoelectric deformations caused by opposed electric field components  $\pm E_{\parallel}$  add up to a net movement of the surface. Thus for a full analysis of the deformation of the sample surface all components of the electric field have to be taken into account. For our analysis we consider exemplarily the 5 principal directions of the electric field choosing the notation such that they follow the crystallographic axes. I. e. when the tip is on top of a  $x$ -face, the electric field component  $E_{\perp}$  is called  $E_x$ . The in plane electric field components  $E_{\parallel}$  are consistently called  $\pm E_y$  and  $\pm E_z$ .

A step-by-step analysis of the deformation of the  $x$ -face can be accomplished as follows (Fig. 5):

- The effect of  $E_x$  on the piezoresponse of the sample due to the longitudinal tensor element  $d_{11}$  can be easily analyzed since for LiNbO<sub>3</sub>  $d_{11} = 0$ , thus the thickness change is  $\Delta x = d_{11} U = 0$ .
- Whereas the electric field component  $+E_z$  causes expansion ( $\Delta z = d_{33} U$ ) the opposed component  $-E_z$  leads to a contraction of the crystal ( $\Delta z = -d_{33} U$ ). As a result a net sliding of the surface along the  $z$ -axis occurs (Fig. 5(a)).
- In an analogous way, the electric field components  $\pm E_y$  excite the longitudinal tensor element  $d_{22}$  which leads to a sliding of the surface along the  $y$ -axis.
- The effect of  $E_x$  on the piezoresponse of the sample due to the shear tensor element  $d_{15}$  is schematically depicted in Fig. 5(b). Such a deformation,

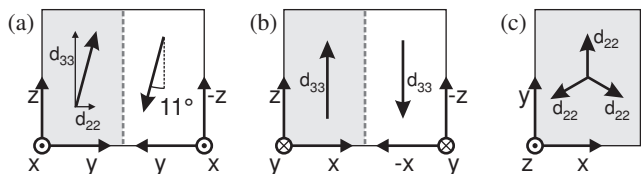


FIG. 6: In-plane displacement of the different surfaces of a LiNbO<sub>3</sub> crystal, shown for a bi-domain crystal. (a) On the  $x$ -face, the contributions from  $d_{22}$  and  $d_{33}$  add up vectorially. (b) On the  $y$ -face, only the  $d_{33}$  tensor component leads to a sliding of the surface. (c) The movement on the  $z$ -face caused by  $d_{22}$  reflects the trigonal symmetry of the material.

however, is strongly suppressed. This can be understood as follows: Within the whole volume experiencing the electric field  $E_x$  the crystals deformation is of same type, e.g. a shear to the right. Since this volume is restricted compression and extraction occurs at its limits leading to clamping. The fact that the electric field  $E_x$  decays with  $1/r^2$  ( $r$ : tip radius) and therefore the limits are not rigid does not play a role. The only difference is that clamping is dispersed along the decay length of the electric field  $E_x$ , the overall effect, however, persists. Note that this situation is very different from the one in Fig. 5(a), where one side wants to contract and the other side wants to expand.

As a result of the considerations listed above, the  $x$ -face performs a sliding movement underneath the tip at an angle of  $\theta = \arctan(d_{22}/d_{33}) = 11^\circ$  relative to the crystallographic  $z$ -axis, inserting the numbers for the piezoelectric tensor elements determined previously (Fig. 6(a)). A contribution of shearing to the surface displacement would lead to another angle. Its precise measurement is thus the key experiment to sustain the proposed model of expansion & contraction and suppressed shearing.

Similar considerations apply for the  $y$ -face (Fig. 6(b)). Note that there is a net thickness change of the sample  $\Delta y = d_{22} U$ . The  $E_{\parallel}$  components of the electric field, lead to  $\Delta x = d_{11} U = 0$  since  $d_{11} = 0$  and  $\Delta z = d_{33} U$  resulting in a net sliding of the surface along the  $z$ -axis.

For the  $z$ -face, there is a net thickness change  $\Delta z = d_{33} U$ , yielding the standard PFM signal. Upon closer inspection, we observed an extremely small piezomechanical in-plane response, reflecting the trifold symmetry of the crystals  $y$ -axes. This movement of the surface can be attributed to the fact that the tip has an inclination with respect to the surface of approx.  $20^\circ$ . This leads to a slightly asymmetric electric field distribution and thus the contributions from the three identical  $y$ -axes of the crystal do not cancel each other. In Fig. 6(c) the in-plane displacements on the three crystal faces of LiNbO<sub>3</sub> are shown.

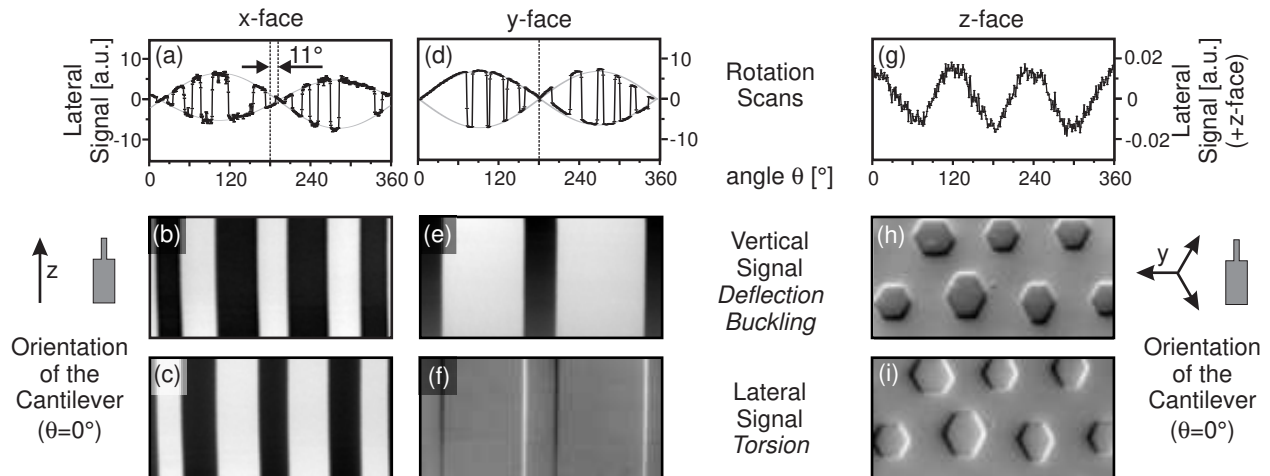


FIG. 7: Top row: Lateral signal during  $360^\circ$  rotation scans on all three faces of the HexLN sample. Center row: vertical image and bottom row: lateral image of the three faces respectively. Left column:  $x$ -face, middle column:  $y$ -face and right column:  $z$ -face. For the  $x$ - and the  $y$ -faces, the angle is defined between the cantilever  $C$  and the  $z$ -axis of the crystal ( $\theta = 0^\circ : C \parallel z$ ). For the  $z$ -face an angle of  $0^\circ$  corresponds to a cantilever being orientated perpendicular to one of the three  $y$ -axes ( $\theta = 0^\circ : C \perp y$ ) Image size for all six images:  $60 \mu\text{m} \times 30 \mu\text{m}$ .

## B. Rotation scans

Figure 7 summarizes our experimental results. We always recorded the vertical and the lateral signal simultaneously, thus (b and c), (e and f), and (h and i) were recorded during the same scan. Obviously, all images show a clear domain contrast, whereas (b,c, and e) show only the domain faces, (f and i) only the domain boundaries, and (h) a combination of both. On every face, we also performed rotation scans, i. e., we rotated the sample by  $360^\circ$  during data acquisition. To clearly attribute the recorded signals to in-plane driving forces, we show the data for the lateral signal (a,d,g). For the  $x$ - and the  $y$ -face, the pivot of the rotation axis was set such that the tip performed a circle of several  $10 \mu\text{m}$  radius on top of the surface. Thereby, we could record the data for both domain faces simultaneously, seen as jumps in the graphs. The scan on the  $z$ -face was performed on a single  $+z$  domain face.

For understanding the content of Fig. 7 we start with the last column depicting the measurements on the  $z$ -face. Fig. 7(h) shows the standard PFM deflection signal, with the  $-z$  faces of the hexagonal domains appearing dark on the bright  $+z$  face. The white borders on the upper edges and the dark ones on the lower edges are due to a buckling movement of the cantilever at the domain boundaries. This is caused by the electrostatic interaction between the charged tip and the electrostatic field at the domain walls. The latter is due to the differently orientated domains carrying surface polarization charges of opposite polarity. In the torsion channel recorded in Fig 7(i) only the domain boundaries are seen. A detailed description of the lateral electrostatic force microscopy can be found elsewhere [33].

The rotation scan on the  $z$ -face (Fig. 7(g)) shows a very

small, but clearly resolvable lateral signal. As expected from the considerations described above, the three maxima reflect the trigonal symmetry of  $\text{LiNbO}_3$  indicating the three identical crystallographic  $y$ -axes.

Investigations of the  $y$ -face of the crystal yield the following results: Upon perfect alignment of the cantilever parallel to the crystallographic  $z$ -axis, the lateral signal shows only the domain boundaries (Fig. 7(f)) due to the electrostatic interactions [33]. Rotating the sample, however, reveals a lateral movement on top of the domain faces, with a maximum at an angle of  $90^\circ$  (Fig. 7(d)). This can be attributed to the sliding of the surface caused by the longitudinal deformation along the  $z$ -axis. Torsion and buckling, however, being caused by the same driving force, their maximum amplitudes occur at an relative angle of  $90^\circ$ . Thus, the contrast in Fig. 7(e) is due to a superposition of (i) a deflection of the cantilever caused by the standard PFM ( $\Delta y = d_{22} U$ ) and (ii) its buckling caused by a sliding along the  $z$ -axes of the crystal.

Finally, figure 7(b) shows the most surprising result: a clear domain contrast on the  $x$ -face of  $\text{LiNbO}_3$ . Although unexpected at first sight (because  $d_{11} = 0$ ), this is consistent with the considerations exposed above. According to our expansion-contraction-model sliding of the surface should occur at an angle of  $\theta = 11^\circ$ . For images taken at  $\theta = 0^\circ$  the cantilever performs both a buckling and a torsion movement as seen in the images in Figs. 7(b and c). The exact angle of the maximum surface displacement could be confirmed by a rotation scan shown in Fig. 7(a) where we found a shift of the zero-crossing of  $11^\circ$ . Note the adjustment of the cantilever axis with respect to the  $z$ -axis is performed by recording large PFM images and is precise to about  $1^\circ$ .

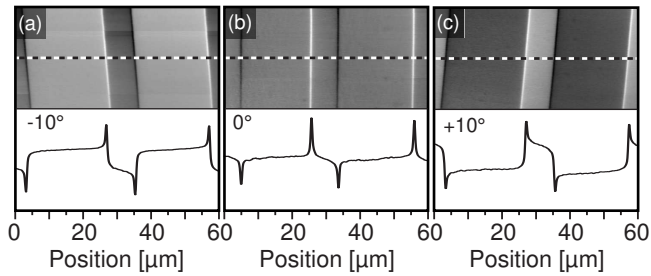


FIG. 8: Lateral signal on a  $y$ -face recorded for three different orientations between cantilever and  $z$ -axis: a)  $-10^\circ$ , b)  $0^\circ$ , and c)  $+10^\circ$ .

### C. Lateral $y$ -face imaging

Finally, a clear demonstration for the contribution of the two different contrast mechanisms to the lateral signal (surface displacement and electrostatic interaction) on a  $y$ -face can be seen in Fig. 8. We therefore recorded three images at different angles between the cantilever axis and the  $z$ -axis of the crystal. With the cantilever oriented parallel to the  $z$ -axis of the crystal only the electrostatic signal at the domain boundaries can be observed (Fig. 8(b)). The line scan shows no contrast of the domain faces. When the sample is rotated by  $-10^\circ$  with respect to the cantilever axis also the domain faces show a contrast due to a contribution of the  $z$ -directed sliding of the surface. Note that the wide domains appear brighter than the narrow ones (Fig. 8(a)). If the sample is rotated by  $+10^\circ$  the projection of the  $z$ -directed movement to the torsion of the cantilever is inverse, thus the wide domains show up as dark stripes while the narrow ones are bright (Fig. 8(c)).

## IV. CONCLUSIONS

In this contribution, we have carried out a thorough investigation of the origin of the domain contrast on all faces of LiNbO<sub>3</sub> single crystals. A clear domain contrast could be observed on all crystal faces, in the vertical as well as in the lateral read-out channel. Upon close inspection, the domain contrast could be attributed to a superposition of three driving forces: (i) standard piezoresponse force microscopy (PFM) originating from a thickness change of the sample, (ii) a piezomechanically caused lateral displacement of the surface due to an expanding-contraction-movement, and (iii) the electrostatic interaction of the charged tip with the electric fields on top of the crystals  $y$ - and  $z$ -faces.

In order to perform these experiments, we upgraded our scanning force microscope (SFM) mounting the samples on a high-precision rotation stage. It has thus become possible to investigate a well defined position on top of the sample surface at different orientations of the cantilever with respect to the sample. This technical issue in combination with the complete understanding of the detection mechanism now allows to determine unambiguously the orientation of the polar axis any arbitrarily orientated ferroelectric particle and for specifically cut piezoelectric samples to determine their symmetry axis.

## V. ACKNOWLEDGMENTS

We thank C. Gawith from the Optoelectronics Research Centre, University of Southampton (UK) for providing the HexLN sample. Financial support of the Deutsche Telekom AG is gratefully acknowledged.

- 
- [1] M. Alexe and A. Gruverman, eds., *Nanoscale Characterisation of Ferroelectric Materials* (Springer, Berlin; New York, 2004) 1st ed.
  - [2] A. Gruverman and S.V. Kalinin, *J. Materials Science* **41**, 107 (2006).
  - [3] S.V. Kalinin, A. Rar, and S. Jesse, *IEEE T. Ultrason. Ferr.* **53**, 2226 (2006).
  - [4] T. Jungk, Á. Hoffmann, and E. Soergel, *New. J. Phys.* **10**, 013019 (2008).
  - [5] R.E. Newnham, *Properties of Materials* (New-York: Oxford University Press 2005) 1st ed.
  - [6] E. Soergel, *Appl. Phys. B* **81**, 729 (2005).
  - [7] C. Canalias, V. Pasiskevicius, A. Fragemann, and F. Laurell, *Appl. Phys. Lett.* **83**, 734 (2003).
  - [8] M. Abplanalp, L.M. Eng, and P. Günther, *Appl. Phys. A* **66**, S231 (1998).
  - [9] L.M. Eng, H.-J. Güntherodt, G.A. Schneider, U. Köpke and J. Muñoz Saldaña, *Appl. Phys. Lett.* **74**, 233 (1999).
  - [10] H.F. Yu, H.R. Zeng, L.N. Zhang, R.Q. Chu, G.R. Li, and Q.R. Yin, *Materials Letters* **59**, 1538 (2005).
  - [11] S. Katayama, Y. Noguchi, and M. Miyayama, *Advanced Materials* **19**, 2552 (2007).
  - [12] H. Okino, T. Ida, H. Ebihara, H. Yamada, K. Matsushige, and T. Yamamoto, *Jpn. J. Appl. Phys.* **40**, 5828 (2001).
  - [13] H. Amarin, V.V. Shvartsman, I.K. Bdikin, M.E.V. Costa, A.L. Kholkin, and N.A. Pertsev, *Appl. Phys. Lett.* **88**, 062903 (2006).
  - [14] M. Abplanalp, D. Barošova, P. Bridenbaugh, J. Erhart, J. Fousek, P. Günther, J. Nosek, and M. Sulk, *J. Appl. Phys.* **91**, 3797 (2002).
  - [15] H.R. Zeng, H.F. Yu, R.Q. Chu, G.R. Li, H.S. Luo, and Q.R. Yin, *J. Cryst. Growth* **267**, 194 (2004).
  - [16] F. Zavaliche, R.R. Das, D.M. Kim, C.B. Eom, S.Y. Yang, P. Shafer, and R. Ramesh, *Appl. Phys. Lett.* **87**, 182912 (2005).
  - [17] B. Gautier and V. Bornand, *Thin Solid Films* **515**, 1592 (2006).
  - [18] C. Loppacher, F. Schlaphof, S. Schneider, U. Zerweck, S. Grafström, L.M. Eng, A. Roelofs, and R. Waser, *Surf. Science* **532**, 483 (2003).
  - [19] H.Z. Zeng, J.S. Liu, L.S. Dai, Z.H. Wang, S.X. Bao, and Y.R. Li, *J. Electroceram.* **15**, 135 (2005).

- [20] S.V. Kalinin, B.J. Rodriguez, S. Jesse, J. Shin, A.P. Baddorf, P. Gupta, H. Jain, D.B. Williams, and A. Gruverman, *Microscopy and Microanalysis* **12**, 206 (2006).
- [21] C.S. Ganpule, V. Nagarajan, B.K. Hill, A.L. Roytburd, E.D. Williams, R. Ramesh, S.P. Alpay, A. Roelofs, R. Waser, and L.M. Eng, *J. Appl. Phys.* **91**, 1477 (2002).
- [22] H.F. Yu, H.R. Zeng, R.Q. Chu, G.R. Li, and Q.R. Yin, *Phys. Stat. Sol. a* **202**, 158 (2005).
- [23] V.V. Shvartsman, W. Kleemann, R. Haumont, and J. Kreisel, *Appl. Phys. Lett.* **90**, 172115 (2007).
- [24] B.J. Rodriguez, A. Gruverman, A.I. Kingon, R.J. Nemanich, and J.S. Cross, *Appl. Phys. Lett.* **95**, 1958 (2004).
- [25] F. Felten and G.A. Schneider and J. Muñoz Saldaña and S.V. Kalinin, *J. Appl. Phys.* **96**, 563 (2004).
- [26] T. Jungk, Á. Hoffmann, and E. Soergel, *Appl. Phys. Lett.* **89**, 042901 (2006).
- [27] Á. Hoffmann, T. Jungk, and E. Soergel, *Rev. Sci. Instrum.* **78**, 016101 (2007).
- [28] *Ferroelectrics and Related Substances*, edited by K.-H. Hellwege and A. M. Hellwege, Landolt-Brnstein III/16 (Springer, Berlin, 1981).
- [29] V. Likodimos, M. Labardi, M. Allegrini, N. Garcia, and V.V. Osipov, *Surf. Sci.* **490**, 76 (2001).
- [30] M. Gouklov, S. Odoulov, Th. Woike, J. Imbrock, M. Imlau, E. Krätzig, C. Bäumer, H. Hesse *Phys. Rev. B* **65**, 195111 (2002)
- [31] P.W. Tasker *J. Phys. C* **12**, 4977 (1979).
- [32] T. Jungk, Á. Hoffmann, and E. Soergel, *Appl. Phys. A* **86**, 353 (2007).
- [33] T. Jungk, Á. Hoffmann, and E. Soergel, *Appl. Phys. Lett.* **89**, 163507 (2006).